

Effect of hydrostatic pressure on the kinetics of alpha–omega phase transformation in zirconium

Brown Jacob, Yeddu Hemantha Kumar

This is a Final draft version of a publication
published by IOP Publishing
in Modelling and Simulation in Materials Science and Engineering

DOI: 10.1088/1361-651X/ac5fc4

Copyright of the original publication:

© 2022 IOP Publishing

Please cite the publication as follows:

J. Brown, H.K. Yeddu. (2022). Effect of hydrostatic pressure on the kinetics of alpha–omega phase transformation in zirconium. Modelling and Simulation in Materials Science and Engineering, 30, p. 045008. DOI: 10.1088/1361-651X/ac5fc4

**This is a parallel published version of an original publication.
This version can differ from the original published article.**

Effect of hydrostatic pressure on the kinetics of alpha – omega phase transformation in zirconium

Jacob Brown^a, Hemantha Kumar Yeddu^{a,b,*}

^a*School of Engineering, Newcastle University, Newcastle upon Tyne, NE1 7RU, United Kingdom.*

^b*Department of Mechanical Engineering, Lappeenranta University of Technology (LUT), 53850 Lappeenranta, Finland.*

Abstract

A three dimensional (3D) elastoplastic phase-field model, including strain hardening, is employed to study the effect of hydrostatic pressure in the range of 4 – 9 GPa on the kinetics of alpha – omega phase transformation in zirconium (Zr). The input data corresponding to pure Zr are acquired from experimental studies as well as by using the CALPHAD method. A decreasing incubation time, for the formation of omega variants, with increasing pressure is observed. Avrami (JMAK) equation is used to study the transformation kinetics by analysing the phase fraction plots predicted by the phase-field simulations. The estimated activation energy is in the range of 54 – 59 kJ/mol and decreases at an average rate of 992 J/mol per 1 GPa increase in pressure. The analysis of Avrami exponents, based on Cahn’s approach, show that the transformation region can be divided into two distinct regions with a change in slope, which is attributed to the site saturation. It is concluded that in the first region where the exponents are above 3, the transformation proceeds by nucleation and growth. In the second region where the exponents are sub-unity, the transformation proceeds by growth of the existing variants.

Keywords: Phase-field method, transformation kinetics, omega phase, microstructure, zirconium

*Corresponding Author. E-mail: hemantha.yeddu@lut.fi; hemu23@gmail.com

Published in *Modelling and Simulation in Materials Science and Engineering* on 13 April 2022. Citation: J. Brown and H.K. Yeddu, *Modelling Simul. Mater. Sci. Eng.* 30 (2022) 045008. doi: 10.1088/1361-651X/ac5fc4.

1. Introduction

Zirconium (Zr) and its alloys are widely used in the nuclear power generation as components in the nuclear reactor due to their good corrosion resistance and mechanical properties. Zr-alloys also possess very low thermal neutron cross section that indicates a low capture rate of neutrons [1]. During their service the reactor components need to withstand a range of temperatures and pressures, which can lead to various phase transformations that in turn alter the mechanical properties of the reactor components.

Different phases, viz. α , β and ω , can form in zirconium (Zr) and its alloys over a range of pressures and temperatures. α transforms to ω under hydrostatic pressure [2–4] or during shock loading [3, 4], whereas at high temperatures the α phase transforms to β phase [5]. The beta (β) phase can transform to ω phase either athermally, isothermally or by stress application in Zr-alloys [4, 6].

The materials (e.g. Zr) used in a nuclear reactor can be subjected to high static pressure, which can induce formation of brittle ω phase from α phase and can affect the mechanical properties of the material. Therefore, it is essential to study the formation of omega phase under a range of pressures using in-situ techniques. However, achieving pure hydrostatic conditions during in-situ experiments can be challenging [7, 8] and can lead to incorrect measurements of transformation start pressures and phase fractions that in turn can lead to incorrect understanding of the transformation kinetics.

Phase-field approach has been proved to simulate microstructure evolution with accurate predictions of several microstructural features. Phase-field approach has been used to study solidification, diffusion-controlled phase transformations, precipitate formation and propagation of cracks [9–14]. Martensitic transformations have been studied extensively using the phase-field method [15–29]. In a previous work by one of the present authors, the alpha (hcp) to omega (hexagonal) phase transformation occurring in a single crystal of pure Zr under hydrostatic pressure was studied using a three dimensional (3D) phase-field model by including plasticity and strain hardening [25].

In the present work, the elastoplastic phase-field model developed in Ref. [25] is employed to study the effect of hydrostatic pressure on $\alpha - \omega$ phase transformation kinetics in Zr. Previous experiments and the analysis of phase fractions using the Avrami equation showed that the study of Avrami ex-

ponent and activation energy can provide insights into the transformation kinetics and dimensionality of the transformation [2]. However, due to lack of high speed in-situ imaging techniques, there are still some unanswered questions with respect to the transformation kinetics and sub-unity Avrami exponents observed [2]. In the present work, we address these questions by providing theoretical insight into the transformation kinetics through the phase-field simulations.

2. Phase-field model

The phase-field equation to model the evolution of martensitic microstructure is given by [16, 17, 25]:

$$\frac{\partial \eta_p}{\partial t} = -L \sum_{p=1}^{p=3} \left(\frac{\partial G_v^{chem}}{\partial \eta_p} + \frac{\partial G_v^{el}}{\partial \eta_p} - \frac{1}{2} \beta \frac{\partial \eta_p}{\partial r_i} \frac{\partial \eta_p}{\partial r_j} \right) \quad (1)$$

where η_p is the phase field variable, $\mathbf{r}(\mathbf{x}, \mathbf{y}, \mathbf{z})$ is the position vector, L is the interfacial kinetic coefficient, G_v^{chem} is the chemical part of the Gibbs energy density and G_v^{el} is the strain energy density. The last term in Eq. (1) is the gradient energy term (G_v^{grad}), where $\beta = \frac{9\gamma^2 V_m}{16\Delta G^*}$ is the gradient energy coefficient, γ is the interfacial energy, ΔG^* is the Gibbs energy barrier and V_m is molar volume.

The α to ω gives rise to three crystallographic orientations (variants) of ω [25]. Thus, in order to model the three omega variants, three phase-field variables (η_1, η_2, η_3) are considered in the model. G_v^{chem} is expressed as a Landau-type polynomial in terms of the three phase-field variables [25]:

$$G_v^{chem}(\eta_1, \eta_2, \eta_3) = \frac{1}{V_m} \left[\frac{1}{2} A (\eta_1^2 + \eta_2^2 + \eta_3^2) - \frac{1}{3} B (\eta_1^3 + \eta_2^3 + \eta_3^3) + \frac{1}{4} C (\eta_1^2 + \eta_2^2 + \eta_3^2)^2 \right] \quad (2)$$

where the coefficients A, B, C are expressed in terms of Gibbs energy barrier (ΔG^*) and the driving force (ΔG_m) as: $A = 32\Delta G^*$, $B = (3A - 12\Delta G_m)$, $C = (2A - 12\Delta G_m)$ and $\Delta G^* = \frac{V_m \beta}{2\delta^2}$ [16]. δ is the physical interface thickness. G_v^{el} is expressed as:

$$G_v^{el} = \int_{\epsilon_{ij}^0(\mathbf{r})}^{\epsilon_{ij}(\mathbf{r})} \sigma_{ij}(\mathbf{r}) d\epsilon_{ij}(\mathbf{r}) \quad (3)$$

where $\epsilon_{ij}^0(\mathbf{r})$ is the stress-free transformation strain, $\epsilon_{ij}(\mathbf{r})$ is the total strain and $\sigma_{ij}(\mathbf{r})$ is the elastic stress. In order to reduce the complexity of the system, isotropic elastic properties are considered in the present work and hence $\sigma_{ij}(\mathbf{r})$ is given by:

$$\sigma_{ij}(\mathbf{r}) = \frac{E}{1+\nu} \left[\epsilon_{ij}^{el}(\mathbf{r}) + \frac{\nu}{1-2\nu} \epsilon_{kk}^{el}(\mathbf{r}) \delta_{ij} \right] \quad (4)$$

where E is Youngs modulus of elasticity and ν is Poisson's ratio. $\epsilon_{kl}^{el}(\mathbf{r})$ is the elastic strain, given by:

$$\epsilon_{kl}^{el}(\mathbf{r}) = \epsilon_{kl}(\mathbf{r}) - \epsilon_{kl}^0(\mathbf{r}) - \epsilon_{kl}^{pl}(\mathbf{r}) \quad (5)$$

where $\epsilon_{kl}^{pl}(\mathbf{r})$ is the plastic strain. Assuming small strain theory, total strain is given by $\epsilon_{ij}(\mathbf{r}) = \frac{1}{2} \left(\frac{\partial u_i(\mathbf{r})}{\partial r_j} + \frac{\partial u_j(\mathbf{r})}{\partial r_i} \right)$. $\mathbf{u}(\mathbf{r})$ is the local displacement vector calculated by solving the mechanical equilibrium equation $\frac{\partial \sigma_{ij}(\mathbf{r})}{\partial r_j} = 0$.

The stress-free transformation strain (SFTS) is given by:

$$\epsilon_{ij}^0(\mathbf{r}) = \sum_{p=1}^{p=v} \eta_p(\mathbf{r}) \epsilon_{ij}^0(p) \quad (6)$$

where $\epsilon_{ij}^0(p)$ is the SFTS tensor corresponding to each variant. By considering the Silcock transformation pathway for the $\alpha - \omega$ transformation [5, 25, 30], the SFTS tensors of the three ω variants are:

$$\begin{aligned} \epsilon_{ij}^0(1) &= \begin{bmatrix} \epsilon_1 & 0 & 0 \\ 0 & \epsilon_2 & 0 \\ 0 & 0 & \epsilon_3 \end{bmatrix}, \quad \epsilon_{ij}^0(2) = \begin{bmatrix} \frac{\epsilon_1+3\epsilon_3}{4} & 0 & \frac{\sqrt{3}(-\epsilon_1+\epsilon_3)}{4} \\ 0 & \epsilon_2 & 0 \\ \frac{\sqrt{3}(-\epsilon_1+\epsilon_3)}{4} & 0 & \frac{3\epsilon_1+\epsilon_3}{4} \end{bmatrix}, \\ \epsilon_{ij}^0(3) &= \begin{bmatrix} \frac{\epsilon_1+3\epsilon_3}{4} & 0 & \frac{\sqrt{3}(\epsilon_1-\epsilon_3)}{4} \\ 0 & \epsilon_2 & 0 \\ \frac{\sqrt{3}(\epsilon_1-\epsilon_3)}{4} & 0 & \frac{3\epsilon_1+\epsilon_3}{4} \end{bmatrix} \end{aligned} \quad (7)$$

where $\epsilon_1 = \frac{c_\omega - a_\alpha}{a_\alpha}$, $\epsilon_2 = \frac{a_\omega - c_\alpha}{c_\alpha}$, $\epsilon_3 = \frac{2\sqrt{3}a_\omega - 3\sqrt{3}a_\alpha}{3\sqrt{3}a_\alpha}$. $a_\alpha, c_\alpha, a_\omega$ and c_ω are lattice constants of α and ω phases, respectively. The SFTS tensors of variants-2 and 3 in Eq. (7) are obtained by using $\epsilon_{ij}^0(2) = A\epsilon_{ij}^0(1)A^T$ and $\epsilon_{ij}^0(3) = A\epsilon_{ij}^0(2)A^T$, where A is rotation matrix given by:

$$A = \begin{bmatrix} \frac{1}{2} & 0 & -\frac{\sqrt{3}}{2} \\ 0 & 1 & 0 \\ \frac{\sqrt{3}}{2} & 0 & \frac{1}{2} \end{bmatrix} \quad (8)$$

The evolution of plastic strain $\epsilon_{ij}^{pl}(\mathbf{r})$ is given by [16, 25]:

$$\frac{\partial \epsilon_{ij}^{pl}(\mathbf{r})}{\partial t} = -k_{ijkl} \frac{\delta G_v^{shear}}{\delta \epsilon_{kl}^{pl}(\mathbf{r})} \quad (9)$$

where G_v^{shear} is the shear energy density that depend on the deviatoric strain components [16], k_{ijkl} ($= kc_{ijkl}^{-1}$) is the plastic kinetic coefficient and c_{ijkl}^{-1} is the compliance tensor. k is plastic relaxation rate that governs the rate at which stresses are relaxed [16]. von Mises yield criterion is considered. Linear isotropic strain hardening is considered by using the expression $\sigma_y = \sigma_y^0 + H\epsilon^{pl}(\mathbf{r})$ [31], where σ_y is the yield stress of the material, σ_y^0 is the initial yield stress, H is the hardening modulus and $\epsilon^{pl}(\mathbf{r})$ is the equivalent plastic strain.

The extra Gibbs energy density G_v^{appl} caused by the externally applied stress is given by [16]:

$$G_v^{appl} = -\sigma_{ij}^{appl} \epsilon_{ij}^0(\mathbf{r}) \quad (10)$$

where σ_{ij}^{appl} is the externally applied Cauchy stress tensor, given by:

$$\sigma_{ij}^{appl} = \begin{bmatrix} \sigma_{xx} & \sigma_{xy} & \sigma_{xz} \\ \sigma_{yx} & \sigma_{yy} & \sigma_{yz} \\ \sigma_{zx} & \sigma_{zy} & \sigma_{zz} \end{bmatrix} \quad (11)$$

2.1. Simulations

In this work the effect of hydrostatic pressure on omega phase formation, transformation kinetics and the microstructure evolution is studied by considering a single crystal of pure Zr at 300 K. The time-dependent phase fractions at various pressures predicted by the simulations are fitted to Avrami's model to analyse the transformation kinetics. Hydrostatic pressures in the range of 4 – 9 GPa are applied by considering $\sigma_{xx} = \sigma_{yy} = \sigma_{zz} = -P$ in Eq. (11), where P is the applied pressure. All the off-diagonal terms in Eq. (11) are considered to be zero.

The input simulation data corresponding to pure Zr, acquired from experiments and CALPHAD, is shown in Table 1 [25]. A pre-existing nucleus of omega phase is considered in the center of the alpha grain of 1 μm size where the initial volume fraction of the omega phase is 0.003. Dirichlet (clamped) boundary conditions are considered. As the non-clamped boundary conditions give rise to a single variant that grows over the entire grain [32], and in

order to simulate the growth of multiple omega variants, clamped boundary conditions are considered in this work. Simulations were performed on a 50 x 50 mesh by using FemLego software [33, 34]. Although a physical interface thickness (δ) of 1 nm is used to calculate the Gibbs energy barrier (ΔG^*) and the gradient coefficient (β), in order to achieve better computational efficiency, the size of each mesh element used in the simulations is 20 nm. L in Eq. (1) is considered to be unity due to the ambiguous experimental data of the martensitic interface mobility.

Table 1: Simulation data.

Driving force = 128 J/mol at 300 K, calculated using Thermo-Calc software with PURE database [35]
Thermodynamic coefficients: A = 2376 J/mol, B = 7128 J/mol, C = 4752 J/mol [16, 25]
Gradient coefficient (β) = 1.06066×10^{-11} J/m [16]
Molar volume (V_m) = $14 \times 10^{-6} m^3/mol$
Interface thickness (δ) = 1 nm [16]
Interfacial energy (γ) = $0.01 J/m^2$ [16]
Lattice constants: $a_\alpha = 3.232 \text{ \AA}$, $c_\alpha = 5.147 \text{ \AA}$, $a_\omega = 5.039 \text{ \AA}$, $c_\omega = 3.136 \text{ \AA}$. [36, 37]
Shear modulus (G) = 36.3 GPa [38], Poisson ratio (ν) = 0.331 [38]
Yield stresses: $\sigma_y^\alpha = 180 \text{ MPa}$, $\sigma_y^\omega = 1180 \text{ MPa}$ [39]
Hardening modulus (H) = 1300 MPa [40]
Plastic relaxation rate (k) = $10 \text{ GPa}^{-1} \text{ s}^{-1}$
Interfacial kinetic coefficient (L) = $1 \text{ m}^3 \text{ J}^{-1} \text{ s}^{-1}$

3. Results and discussion

3.1. Phase-field simulations

The phase-field simulations (Fig. 1) show that the pre-existing spherical nucleus of variant-1 (in red) initially dissolves ($\eta < 0.5$) due to the large internal stresses that dominate the available thermodynamic driving force. After some time, the nucleus adjusts its size ($\eta > 0.5$) and shape and grows into a disc-like unit. This shape is the result of the material's attempt to

find a balance between the thermodynamic driving force and the mechanical energy. The mechanical energy is due to the internal stresses developed in the material during the phase transformation. In order to minimize the internal stresses, other variants (in blue and green) nucleate and grow (Figs. 1b – e). The nucleation of new variants ceases as the strain energy is minimized to a certain extent and beyond this point the energy is minimized through growth of the existing omega variants (Figs. 1e – f). This process continues until the strain energy is minimized and the material reaches equilibrium.

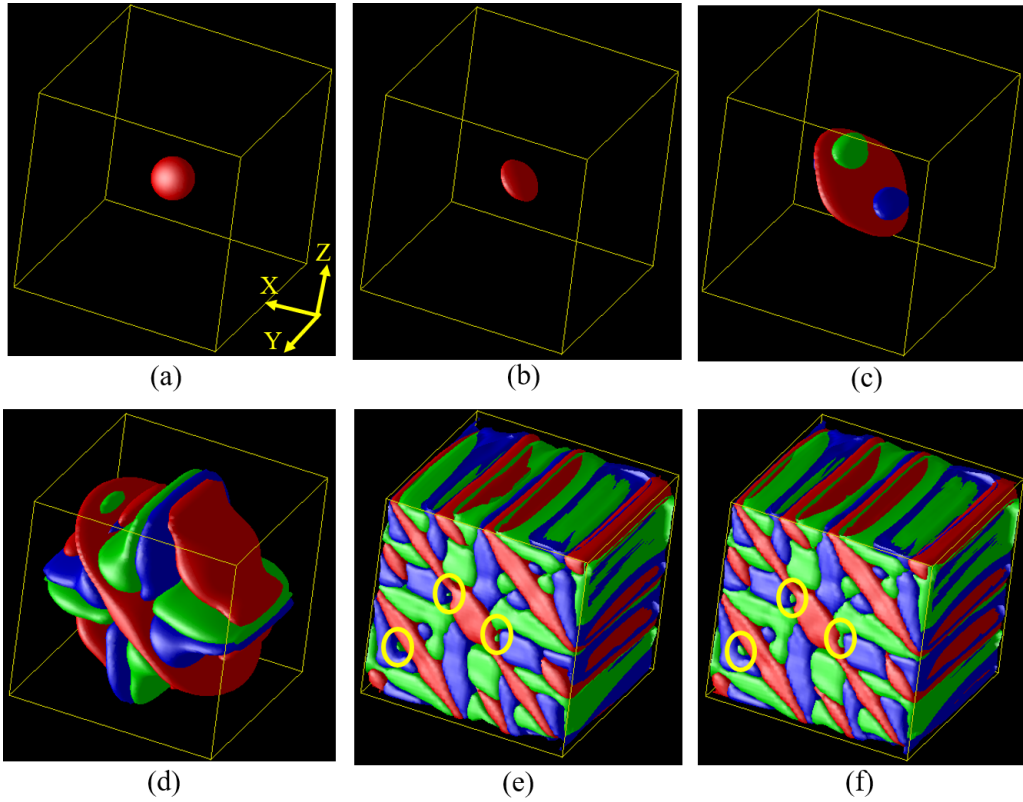


Figure 1: Microstructure evolution in an alpha Zr grain of 1 micron under an applied pressure of 5 GPa at (a) $t^*=0$ (b) $t^*=25$ (c) $t^*=35$ (d) $t^*=50$ (e) $t^*=100$ (f) $t^*=125$. Red, blue and green colors represent omega variants - 1, 2 and 3, respectively. t^* is dimensionless time.

In order to study the effect of the prior alpha grain size on the microstructure, an alpha grain of 2 microns is considered and a hydrostatic pressure of 5 GPa is applied. The resultant microstructure is shown in Fig. 2. As the

final microstructures in Figs. 1f and 2c are very similar, the effect of grain size on the microstructure is negligible.

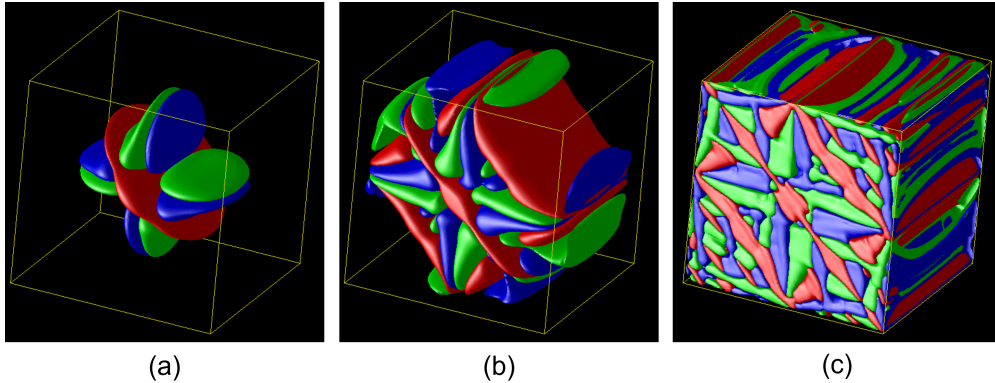


Figure 2: Microstructure evolution in an alpha Zr grain of 2 microns under an applied pressure of 5 GPa at (a) $t^*=35$ (b) $t^*=50$ (c) $t^*=100$.

The volume fraction plots (Fig. 3) predicted by the phase-field simulations at lower pressures (4 and 5 GPa) display the characteristic ‘S-shape’ curve, representing slow transformation rates in the initial and end stages of the process with a rapid and constant intermediary stage. This shape occurs due to the initial time required for the nucleus to form and grow. The rapid intermediary stage represents the nucleation and growth of several variants. The final slow growth stage is due to the deceleration of the transformation due to the dearth of untransformed material or due to the material reaching an equilibrium.

The volume fraction of omega phase increases with increasing time. However, the aforementioned asymptotic relationship at the beginning and end of the transformation may limit the final amount of transformed material to less than 100 %. Similarly, this asymptotic relationship can present an ‘incubation time’, whereby the amount of transformed material is zero until after a time where $t > 0$. The simulations show that incubation time is needed before the transformation can start at lower pressures (Fig. 3). This is in agreement with the general theory that the nuclei of the product phase exist within the homogeneous parent phase at lower pressures, however they do not grow instantaneously at the transformation start pressure. The nuclei will take some time to attain potency, i.e. to attain critical size as well as optimum shape and orientation, and grow when the driving force is

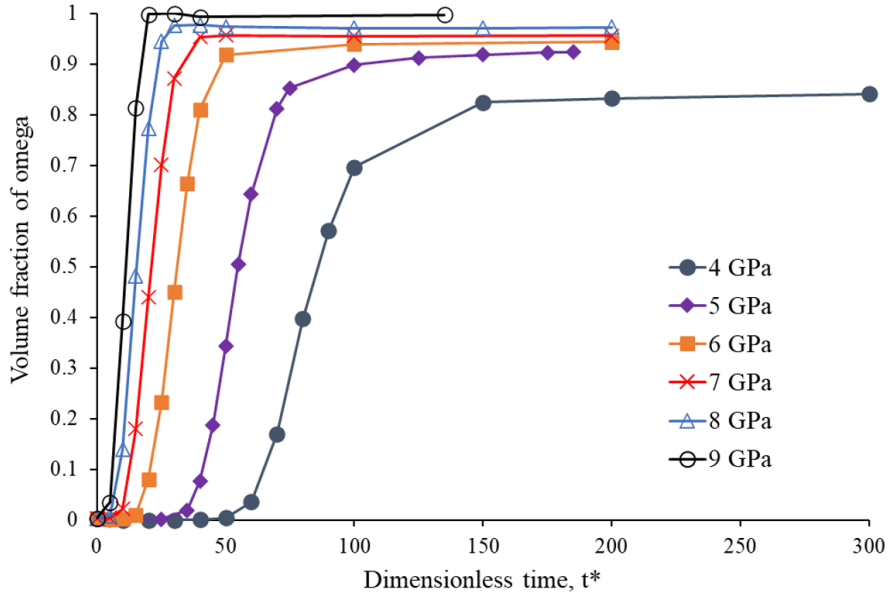


Figure 3: Evolution of omega phase fraction with dimensionless time (t^*) at various pressures.

sufficient to overcome the local stress conditions and thermodynamic energy barrier [41]. As the driving force for phase transformation is relatively lower at lower applied pressure compared to that at higher applied pressure, the time required for the nucleus to attain potency and grow after adjusting to the local stress conditions is longer. At higher applied pressures, due to the large driving force the nucleus can overcome the local stress conditions and thermodynamic energy barrier relatively quickly and hence the incubation time is shorter. Therefore, the incubation time decreases with increasing pressure.

The final volume fraction of omega increases with increasing pressure, reaching 100% under 9 GPa. As the driving force is larger at higher applied pressures, many new variants form already during initial stages of the transformation and create stress fields that lead to self-nucleation of more new variants (Fig. 4a). These variants coarsen during the later stages of the transformation. Due to this interplay of large driving force and self-accommodation mechanisms, the final volume fraction is nearly 100% at higher applied pressures. As the driving force is smaller at lower applied pressures, a smaller number of variants form during the initial stages (Fig.

4b). During the later stages of the transformation, these relatively less number of variants coarsen leading to an omega phase fraction less than 100% by the time the material reaches equilibrium.

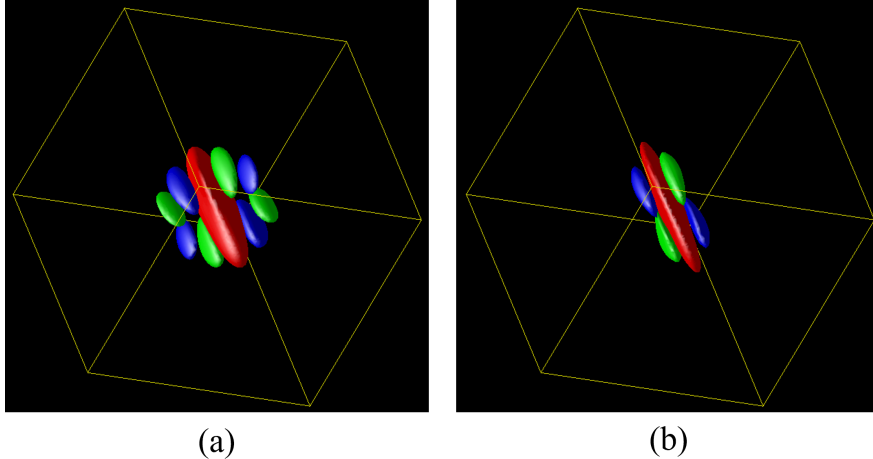


Figure 4: Formation of multiple variants in an alpha Zr grain of 1 micron under an applied pressure of (a) 7 GPa at $t^* = 10$ and (b) 5 GPa at $t^* = 35$.

These results show that the transformation is dependent on activation energy, in agreement with experimental results [2]. The activation energy is estimated by analysing the simulated phase fraction plots by using the Johnson-Mehl-Avrami-Kolmogorov (JMAK) model [42], as explained in the following section.

3.2. Analysis of transformation kinetics using JMAK model

The JMAK model [2, 42–44] predicts time-dependent phase transformations, based on the process of nucleation. In this model, isothermal conditions are assumed to study the kinetics of alpha–omega phase transformation in Zr under hydrostatic pressure. The JMAK equation is expressed as:

$$v = (1 - \exp\{-(t/\tau)^n\}) \quad (12)$$

where v is the omega phase fraction, t is the time, τ is the time when the phase fraction is 63% [43, 44] and n is Avrami exponent.

Eq. (12) needs to be modified in order to analyse the simulated phase fractions using the JMAK model. The pre-factor (A in Eq. (13)) is included in the modified JMAK equation to limit the maximum value of the final phase

fraction. The pre-factor is set equal to the final volume fraction of omega phase predicted by the phase-field simulations. The incubation time needed for the transformation to start, which is significant at lower pressures needs to be included in Eq. (12). With the inclusion of pre-factor and incubation time (t_0), the JMAK equation is expressed as:

$$v = A(1 - \exp\{-K_a((t - t_0)/\tau)^n\}) \quad (13)$$

where t_0 is the incubation time and $K_a = 3.5$ is a fitting parameter that is constant for all the pressure values studied in this work. The other model parameters are shown in Table 2. The resultant JMAK plots fit well with the phase-field results (Fig. 5).

Table 2: Input data used in JMAK model for different hydrostatic pressures (in GPa). Time (t_0 and τ) is dimensionless.

Pressure	A	t_0	τ	n
4	0.846	41	95	2.1
5	0.923	24	59	2.4
6	0.943	12	34	2.7
7	0.955	9	23.5	2.2
8	0.955	5	18.5	2.5
9	0.997	4	13	2.6

The activation energies can be estimated based on the analysis by Singh et al. [43, 44] using:

$$\ln(\tau) = b_0 + \frac{Q}{RT} \quad (14)$$

where b_0 is a constant, Q is the activation energy, R is the gas constant, $T(= 300K)$ is the temperature and τ is the time when the omega phase fraction is 63% [43, 44]. In the absence of activation energy ($Q=0$), it can be assumed that the transformation occurs instantaneously, i.e. at $t^* = \tau = 1$. Using the relation $t^* = tLRT/V_m$ [25], the real time t needed for completion of transformation in a 1 micron grain can be estimated as 5.31×10^{-9} seconds. Using these data, b_0 is estimated as -18.998 , which is constant for all the pressure values studied in this work. Using $b_0 = -18.998$ and τ values shown in Table 2, the activation energies are estimated. These activation energy values (Q) include both the chemical (ΔG^* in Sec. 2) and mechanical energy barriers created by the evolving internal stresses. As shown in Fig. 6,

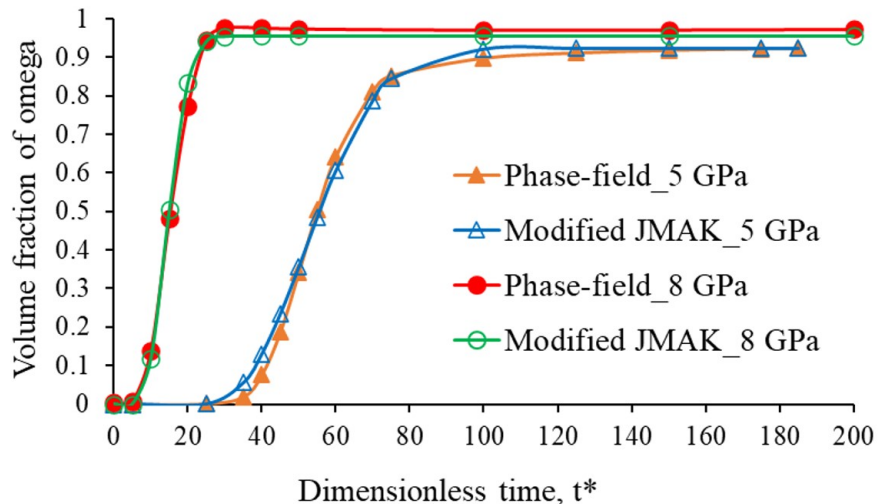


Figure 5: Comparison of phase-field results with the modified JMAK plots.

the activation energies decrease with increasing pressure, in agreement with [2, 43, 44]. The activation energy decreases at an average rate of 992 J/mol per 1 GPa increase in pressure. The incubation time decreases with increasing pressure showing that larger the applied pressure faster is the formation and growth of nuclei. The time constant τ decreases with increasing pressure.

Previous research reported that the exponent n in Eq. (13) is an integer between 1 and 4, which is related to the growth stage of the product phase [2, 42]. Therefore, n represents the dimensionality. The value of Avrami exponent is increased by one to represent a constant nucleation, e.g. three dimensional (3D) growth with a constant nucleation rate would be represented by $n = 4$. However, if the nuclei were preformed, i.e. present prior to the beginning of the transformation, it is represented by $n = 3$. However, the earlier notion that n is an integer has been disproved by experimental data which shows that Avrami exponent n can be of a decimal value [2].

The present analysis based on Eq. (13) results in an exponent value in the range of 2.1 – 2.7 (Table 2). The estimated n values indicate that the transformation is three dimensional [42], which is also evident by the simulated microstructures (Fig. 1). The simulated variants are disc-like where the growth occurs mainly in two directions (longitudinal and lateral) and comparatively less growth occurs in the thickness direction as shown in Fig. 1.

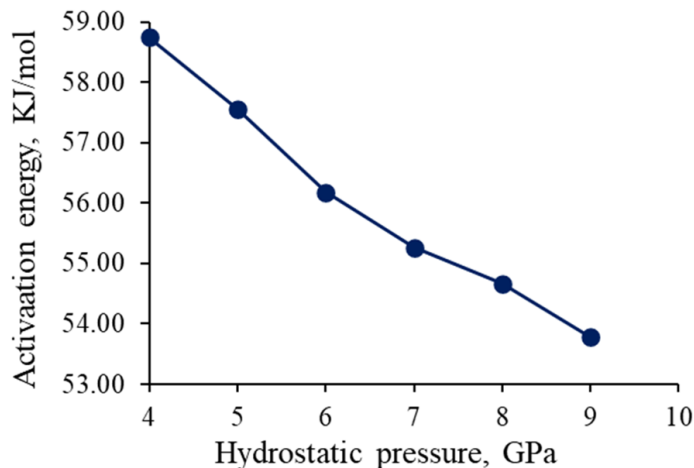


Figure 6: Variation of activation energy with hydrostatic pressure.

Another method to analyse the Avrami exponents n , proposed by Cahn [45], is also used. In this method $\ln(t^*)$ vs $\ln(\ln(1/(1-V_f)))$ are plotted (Fig. 7), where the slopes of these plots yield the n values. t^* is the dimensionless time and V_f is the volume fraction of omega. This analysis shows that the transformation region can be divided into two distinct regions with a change in slope (Fig. 7). The change in slope is due to site saturation, i.e. lack of available nucleation sites [45]. In the first region the exponent ranges between 3.86 – 3.18 and in the second region the exponent is sub-unity (Table 3). Sung and Burns reported an exponent value of 4 before site saturation and 1 after site saturation [46]. A change in exponent value before and after site saturation is in agreement with Sung and Burns, although an exponent value of 1 after site saturation is not observed in this work. However, the present results are in good agreement with Jacobsen et al., who observed sub-unity exponents during the second region of the transformation [2].

The exponent value in the first region decreases with increasing pressure (Table 3 and Fig. 7). A decreasing exponent has been interpreted as decreasing dimensionality and increased spontaneity of the transformation [2]. The phase-field simulations do not show decreasing dimensionality with increasing pressure, although an increased spontaneity can be observed (Fig. 3). An exponent in this range indicates a mixed nature of growth, i.e. a majority of 3D growth but some 2D (planar) growth [2].

Sub-unity exponents are observed (Table 3 and Fig. 7) during the later

Table 3: Exponent (n) values estimated using Cahn’s analysis [45] for different hydrostatic pressures (in GPa).

Pressure	n	
	First region	Second region
4	3.858	0.062
5	3.761	0.395
6	3.83	0.097
7	3.65	0.003
8	3.446	-0.028
9	3.184	0.136

stages of the transformation, i.e. when the volume fraction is above 80%. As demonstrated by the phase-field simulations (Fig. 1e – f), nucleation of new omega variants is not observed beyond this stage of the transformation, indicating site saturation [45]. The transformation progresses mainly through growth of the existing omega variants. As majority of the grain volume is filled with omega phase, the lack of space also contributes to the change in the exponent compared to the initial stage. The simulations show that during this stage, the untransformed alpha phase present in between the omega variants transforms to omega phase (ellipses in Fig. 1e – f). We do not observe isolated transformations in a sea of untransformed material, as suggested in Ref. [2]. Based on this discussion, it can be summarized that when the exponent is above 3, the transformation proceeds by nucleation and growth whereas when the exponent is sub-unity the transformation proceeds by growth of the existing variants.

Our analysis, based on Cahn’s method, shows that the exponent decreases with increasing pressure in the first region. The simulations show that the incubation time decreases with increasing pressure, which indicates an increased spontaneity with increasing pressure, in good agreement with Ref. [2].

4. Conclusions

A 3D elastoplastic phase-field model has been used to study the microstructure evolution during alpha to omega phase transformation in Zr under hydrostatic pressure in the range of 4 – 9 GPa. The simulations show that disc-like omega variants are formed initially, which then grow as laths.

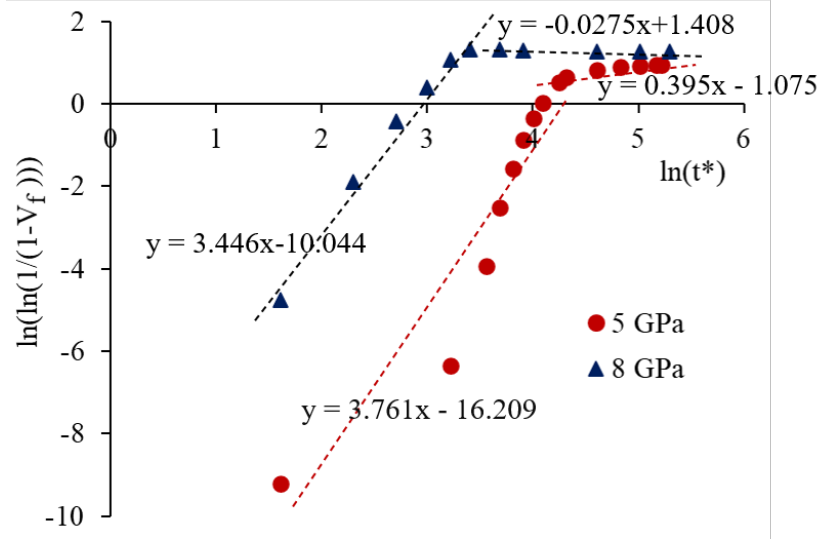


Figure 7: Estimation of JMAK exponents based on Cahn's method [45].

Several new omega variants nucleate and grow in order to minimize the internal stresses developed due to the phase transformation.

At lower pressures (4 – 5 GPa), the volume fraction versus time plots show the typical S-shaped curves. A significant incubation time is needed at lower pressures. A decreasing incubation time with increasing pressure is observed. These results showed the time-dependent nature of the transformation. The volume fraction plots are analysed using a modified JMAK model by including the incubation time and a pre-factor. The activation energy of the transformation at different pressures is estimated. The activation energy decreases at an average rate of 992 J/mol per 1 GPa increase in pressure.

The analysis of Avrami exponents from the JMAK model are in the range of 2.1 – 2.7, indicating that the transformation is three dimensional. The simulated microstructures show that the growth is dominant in two directions giving rise to a disc-like shape with relatively less growth in the thickness direction. Analysis of transformation kinetics, based on Cahn's method, yielded an Avrami exponent in the range of 3.86 – 3.18. The exponent decreased with increasing pressure indicating increased spontaneity of the transformation. This analysis also showed that the transformation region can be divided into two distinct regions with a change in slope, which is attributed to the site saturation. The exponents are above 3 in the first region, where the transformation proceeds by nucleation and growth. The exponents are

sub-unity in the second region, where the transformation proceeds by growth of the existing variants.

Acknowledgements

This work made use of the HPC facilities at Newcastle University. The authors wish to acknowledge CSC – IT Center for Science, Finland, for computational resources.

Conflict of interest

The authors declare that they have no conflicts of interest.

References

- [1] S.F. Mughabghab, Thermal neutron capture cross sections resonance integrals and g-factors, (INDC(NDS)–440), International Atomic Energy Agency (IAEA), (2003).
- [2] M.K. Jacobsen, N. Velisavljevic and S.V. Sinogeikin, Pressure-induced kinetics of the alpha to omega transition in zirconium, *J. Appl. Phys.* 118 (2015) 025902, 1–11.
- [3] R. Tewari, D. Srivastava, G.K. Dey, J.K. Chakravarty, S. Banerjee, Microstructural evolution in zirconium based alloys, *J. Nucl. Mat.* 383 (2008) 153-171.
- [4] S. Banerjee, R. Tewari, G.K. Dey GK, Omega phase transformation - morphologies and mechanisms, *Int. J. Mat. Res.* 97 (2006) 963-977.
- [5] H.R. Wenk, P. Kaercher, W. Kanitpanyacharoen, E. Zepeda-Alarcon, Y. Wang, Orientation relations during the alpha - omega phase transition of zirconium: in situ texture observations at high pressure and temperature, *Phys. Rev. Lett.* 111 (2013) 195701.
- [6] D. Ping, Review on omega phase in body-centered cubic metals and alloys, *Acta Metall. Sin.* 27 (2014) 1-11.
- [7] S.K. Sikka, Y.K. Vohra, R. Chidambaram, Omega phase in materials, *Prog. Mat. Sci.* 27 (1982) 245-310.

- [8] D. Errandonea, Y. Meng, M. Somayazulu, D. Hausermann, Pressure-induced alpha - omega transition in titanium metal: a systematic study of the effects of uniaxial stress, *Physica B* 355 (2005) 116-125.
- [9] N. Moelans, B. Blanpain, P. Wollants, An introduction to phase-field modeling of microstructure evolution, *CALPHAD* 32 (2008) 268–294.
- [10] L.Q. Chen, Phase-field models for microstructure evolution, *Annu. Rev. Mater. Res.* 32 (2002) 113-140.
- [11] S. Minamoto, S. Nomoto, A. Hamaya, T. Horiuchi, S. Miura, Microstructure simulation for solidification of magnesium-zinc-yttrium alloy by multi-phase-field method coupled with CALPHAD database, *ISIJ Int.* 50 (2010) 1914-1919.
- [12] X.H. Guo, S.Q. Shi, X.Q. Ma, Elastoplastic phase field model for microstructure evolution, *Appl. Phys. Lett.* 87 (2005) 221910.
- [13] X.H. Guo, S.Q. Shi, Q.M. Zhang, X.Q. Ma, An elastoplastic phase-field model for the evolution of hydride precipitation in zirconium. Part I: Smooth specimen, *J. Nucl. Mat.* 378 (2008) 110-119.
- [14] J. Bair, M. Asle Zaeem, M. Tonks, A review on hydride precipitation in zirconium alloys, *J. Nucl. Mater.* 466 (2015) 12–20.
- [15] A.G. Khachaturyan, *Theory of Structural Transformations in Solids*, Dover Publications, New York; 2008.
- [16] H.K. Yeddu, A. Borgenstam, J. Ågren, Stress-assisted martensitic transformations in steels: A 3-D phase-field study, *Acta Mater.* 61 (2013) 2595-2606.
- [17] A. Artemev, Y. Jin, A.G. Khachaturyan, Three-dimensional phase field model of proper martensitic transformation, *Acta Mater.* 49 (2001) 1165-1177.
- [18] Y. Wang, A.G. Khachaturyan, Three-dimensional field model and computer modeling of martensitic transformations, *Acta Mater.* 45 (1997) 759-773.

- [19] H.K. Yeddu, T. Lookman, Phase-field modeling of the beta to omega phase transformation in Zr–Nb alloys, *Mater. Sci. Eng. A* 634 (2015) 46–54.
- [20] A. Yamanaka, T. Takaki, Y. Tomita, Elastoplastic phase-field simulation of self- and plastic accommodations in Cubic – tetragonal martensitic transformation, *Mater. Sci. Eng. A* 491 (2008) 378-384.
- [21] R. Ahluwalia, T. Lookman, A. Saxena, R.C. Albers, Landau theory for shape memory polycrystals, *Acta Mater.* 52 (2004) 209-218.
- [22] E.C.H.C. O’Brien, H.K. Yeddu, Multi-length scale modeling of carburization, martensitic microstructure evolution and fatigue properties of steel gears, *J. Mater. Sci. Tech.* 49 (2020) 157–165.
- [23] M. Javanbakht, V.I. Levitas, Phase field simulations of plastic strain-induced phase transformations under high pressure and large shear, *Phys. Rev. B* 94 (2016) 214104.
- [24] J. Kundin, D. Raabe, H. Emmerich, A phase-field model for incoherent martensitic transformations including plastic accommodation processes in the austenite, *J. Mech. Phys. Solids* 59 (2011) 2082-2102.
- [25] H.K. Yeddu, H. Zong, T. Lookman, Alpha–omega and omega–alpha phase transformations in zirconium under hydrostatic pressure: A 3D mesoscale study, *Acta Mater.* 102 (2016) 97–107.
- [26] M. Javanbakht and E. Barati, Martensitic phase transformations in shape memory alloy: phase field modelling with surface tension effect, *Comp. Mater. Sci.* 115 (2016) 137–144.
- [27] M. Mamivand, M.A. Zaeem, H.E. Kadiri, Shape memory effect and pseudoelasticity behavior in tetragonal zirconia polycrystals: A phase field study, *Int. J. Plast.* 60 (2014) 71-86.
- [28] H.K. Yeddu, M.A.J. Somers, Effect of thermal cycling on martensitic transformation and mechanical strengthening of stainless steels—A phase-field study, *Mater. Sci. Eng. A* 690 (2017) 1–5.
- [29] T.W. Heo, L.Q. Chen, Phase-field modeling of displacive phase transformations in elastically anisotropic and inhomogeneous polycrystals, *Acta Mater* 76 (2014) 68-81.

- [30] H. Zong, T. Lookman, X. Ding, C. Nisoli, D. Brown, S.R. Niezgod, S. Jun, The kinetics of the alpha to omega phase transformation in Zr, Ti: Analysis of data from shock-recovered samples and atomistic simulations, *Acta Mater.* 77 (2014) 191–199.
- [31] E.A. De Souza Neto, D. Peric, D.R.J. Owen, *Computational methods for plasticity-Theory and applications*, John Wiley and Sons Ltd., West Sussex (UK), 2008.
- [32] H.K. Yeddu, A. Malik, J. Ågren, G. Amberg, A. Borgenstam, Three-dimensional phase-field modeling of martensitic microstructure evolution in steels, *Acta Mater.* 60 (2012) 1538–1547.
- [33] G. Amberg, R. Tönhardt, C. Winkler, Finite element simulations using symbolic computing, *Math. and Comp. in Simul.* 49 (1999) 257-274.
- [34] M. Do-Quang, W. Villanueva, I. Singer-Loginova, G. Amberg, Parallel adaptive computation of some time-dependent materials-related microstructural problems, *Bull. Pol. Acad. Sci-Tech. Sci.* 55 (2007) 229-237.
- [35] www.thermocalc.com. Accessed on 25.1.2022.
- [36] Y.K. Vohra, Kinetics of phase transformations in Ti, Zr and Hf under static and dynamic pressures, *J. Nucl. Mat.* 75 (1978) 288-293.
- [37] B. Olinger, J.C. Jamieson, Zirconium: phases and compressibility to 120 kilobars, *High Temp. - High Pressures* 5 (1973) 123-131.
- [38] W. Liu, B. Li, L. Wang, J. Zhang, Y. Zhao, Simultaneous ultrasonic and synchrotron x-ray studies on pressure induced alpha-omega phase transition in zirconium, *J. Appl. Phys.* 104 (2008) 076102.
- [39] Y. Zhao, J. Zhang J, Enhancement of yield strength in zirconium metal through high-pressure induced structural phase transition, *Appl. Phys. Lett.* 91 (2007) 201907.
- [40] S.R. Chen, G.T. Gray III, Influence of twinning on the constitutive responses of Zr: experiments and modeling, *J. Phys. IV France* 7 (1997) C3-741-746.

- [41] H.K. Yeddu, A. Borgenstam, J. Ågren, Effect of martensite embryo potency on the martensitic transformations in steels – A 3D phase-field study, *J. Alloys. Compd.* 577S (2013) S141–S146.
- [42] M. Avrami, *J. Chem. Phys.* 8, 212 (1940).
- [43] A.K. Singh, The kinetics of pressure-induced polymorphic transformations, *Bull. Mater. Sci.* 5:3–4 (1983) 219–230.
- [44] A.K. Singh, M. Mohan, C. Divakar, Pressure-induced alpha-omega transformation in titanium: Features of the kinetics data, *J. Appl. Phys.* 54 (1983) 5721–5726.
- [45] J. Cahn, The kinetics of grain boundary nucleated reactions, *Acta Metallurgica*, vol. 4, no. 5, pp. 449-459, 1956.
- [46] C.M. Sung and R.G. Burns, Kinetics of high pressure phase transformations: Implications to the evolution of the olivine – spinel transition in the downgoing lithosphere and its consequences on the dynamics of the mantle, *Tectonophys.*, 31 (1976) 1-32.